Inorganic Chemistry

pubs.acs.org/IC

Article

Structural Properties of $NdTiO_{2+x}N_{1-x}$ and Its Application as Photoanode

Zili Ma,* Kaixuan Chen, Aleksander Jaworski, Jianhong Chen, Anna Rokicińska, Piotr Kuśtrowski, Richard Dronskowski, and Adam Slabon*

Cite This: *Inorg. Chem.* 2021, 60, 919–929

Read Online

ACCESS | Metrics & More | Article Recommendations | Supporting Information

ABSTRACT: Mixed-anion inorganic compounds offer diverse functionalities as a function of the different physicochemical characteristics of the secondary anion. The quaternary metal oxynitrides, which originate from substituting oxygen anions (O^{2-}) in a parent oxide by nitrogen (N^{3-}), are encouraging candidates for photoelectrochemical (PEC) water splitting because of their suitable and adjustable narrow band gap and relative negative conduction band (CB) edge. Given the known photochemical activity of $LaTiO_2N$, we investigated the paramagnetic counterpart $NdTiO_{2+x}N_{1-x}$. The electronic structure was explored both experimentally and theoretically at the density functional theory (DFT) level. A band gap (E_g) of 2.17 eV was determined by means of ultraviolet−visible (UV−vis) spectroscopy, and a relative negative flat band potential of −0.33 V vs reversible hydrogen electrode (RHE) was proposed via Mott−Schottky measurements. ^{14}N solid state nuclear magnetic resonance (NMR) signals from $NdTiO_{2+x}N_{1-x}$ could not be detected, which indicates that $NdTiO_{2+x}N_{1-x}$ is berthollide, in contrast to other structurally related metal oxynitrides. Although the bare particle-based photoanode did not exhibit a noticeable photocurrent, Nb_2O_5 and CoO_x overlayers were deposited to extract holes and activate $NdTiO_{2+x}N_{1-x}$. Multiple electrochemical methods were employed to understand the key features required for this metal oxynitride to fabricate photoanodes.

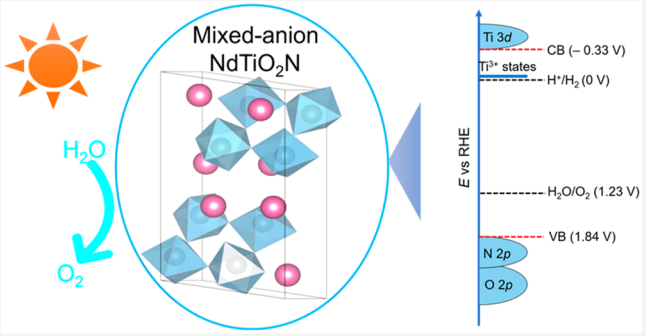

INTRODUCTION

The globally increasing energy demand, which has been mostly met by fossil fuels up to now, is an important challenge. Developing generation IV nuclear technology of high energy density in combination with "renewable" energy of lower density is currently considered a promising strategy for matching that challenge. With respect to the utilization of solar energy to produce alternative fuels, photoelectrochemical (PEC) technology looks like a sustainable solution by splitting water into "green" energy carrier hydrogen under sunlight irradiation, irrespective of the additional challenge to store and ship hydrogen.[1] To improve the efficiency of PEC cells, attempts have been extensively explored since the pioneering conception of water splitting over semiconducting TiO_2.[2]

Serving as the core components of a PEC cell, the semiconducting photoelectrodes responsible for capturing energy from sunlight drive the separation of holes and electrons for consecutive oxidation and reduction of water. The slow kinetics of the oxygen evolution reaction (OER) over n-type photoanodes has motivated scientists to explore materials to address these pivotal issues.[3] The most investigated n-type oxide-based semiconductors have, however, a more positive conduction band (CB) edge than the reduction potential for H^+/H_2, resulting in a high overpotential for OER.[4] Hence, the relatively positive CB position inherently requires more external bias to realize PEC water splitting.

Beyond metal oxides, mixed-anion inorganic compounds, such as oxyfluorides, oxynitrides, oxide−carbodiimides, oxysulfides, oxyhalides, and oxyhydrides, could offer diverse functionalities originating from the different properties of the secondary anion.[5−8] Within the past two decades, transition-metal oxynitrides have emerged as promising photoactive materials because of their frequently higher theoretical solar-to-hydrogen efficiency. This is in particular promising for the quaternary metal oxynitrides because they can exhibit a smaller band gap than the ternary oxides and even than the binary nitride Ta_3N_5 (E_g = 2.1 eV). The less electronegative element N and its more covalent interaction with the metal orbitals as compared to the O 2p orbitals induce an upward shift of the

Received: October 13, 2020
Published: December 29, 2020

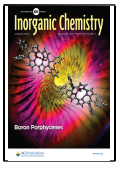

https://dx.doi.org/10.1021/acs.inorgchem.0c03041
Inorg. Chem. 2021, 60, 919−929

valence band (VB) in such compounds, resulting in higher light absorption capability toward the wide visible range.[9−11] Domen et al. have demonstrated a niobium-based oxynitride $BaNbO_2N$ photoanode with photoexcitation up to 740 nm.[12] It should be noted that different anion ordering will affect the band gap varying up to 0.6 eV, which was proven previously on the example of $CaTaO_2N$.[13] The proper band edge positions of quaternary oxynitrides generally straddle the redox potential of water, thereby making them promising visible-light-induced photoelectrodes for overall water splitting.[14] Their negative CB edge positions give negative photocurrent onset potential, which makes metal oxynitrides generally interesting for photoelectrosynthetic cells.[15−17]

The quaternary metal oxynitrides of general formula $AB(O,N)_3$ (A = alkaline-earth metal, lanthanide; B = Ta, Nb, Ti) can exhibit different properties depending on their chemical composition. They are part of a large perovskite-like class of compounds whose synthesis, characterization, properties, and theory have been reviewed quite a while ago.[18] The alkaline-earth-metal tantalum-based oxynitrides $CaTaO_2N$, $SrTaO_2N$, and $BaTaO_2N$ crystallize in different space-group symmetries, that is, orthorhombic, tetragonal, and cubic, as a result of the structural distortion factor caused by the cation radius;[9] in contrast to that averaged structural description by X-ray diffraction which always suffers from the tiny scattering contrast between N and O, there are strong indications, from both first-principles electronic-structure calculations and molecular dynamics simulations, that the local site symmetries are lower, for example, corresponding to orthorhombic symmetry for all the three compounds throughout, including their niobium-based counterparts.[18,19] While their conduction band edge positions differ up to 0.82 eV, the bottom of the conduction band has been proposed to consist entirely of empty Ta 5d orbitals, not too surprising for pentavalent tantalum.[9,20] In comparison to tantalum-based and niobium-based oxynitrides, the titanium-based quaternary oxynitrides, except $LaTiO_2N$, have rarely been investigated for PEC applications.[21] A study by Woodward et al. has shown that $NdTiO_{2+x}N_{1-x}$ and $LaTiO_2N$ crystallize in different space groups but exhibit similar photocatalytic activity for water splitting, which is better than for $CeTiO_2N$ and $PrTiO_2N$.[22] Because the PEC performance is sensitive to the band alignment of the CB and VB edges with respect to the water redox potentials, we were interested to investigate the structural properties of $NdTiO_{2+x}N_{1-x}$ and explore its PEC water splitting activity.

EXPERIMENTAL SECTION

Synthesis of $NdTiO_{2+x}N_{1-x}$. The $Nd_2Ti_2O_7$ oxide precursor was conventionally synthesized by the solid-state reaction (SSR) with KCl as a flux. In a typical synthesis, 1.5 mmol of Nd_2O_3 (99.999 wt %, Koch-Light Laboratories Ltd.), 3 mmol of TiO_2 (99.3 wt %, VWR Chemicals), and 15 mmol of KCl (99.5 wt %, Grüssing GmbH) were mixed and ground, followed by heating in air at 1423 K for 8 h. The product was cooled to room temperature and washed thoroughly with distilled water to remove residual flux. The dried $Nd_2Ti_2O_7$ precursor was placed into an alumina crucible and put in a tube furnace. The thermal ammonolysis was performed under a constant flow of NH_3 (15 mL min^{-1}) and H_2 (5 mL min^{-1}) at 1223 K for 15 h at a ramping rate of 10 K min^{-1}. This ammonolysis process was repeated three times with intermittent grindings.[22]

Fabrication of $NdTiO_{2+x}N_{1-x}$ Photoanodes. The $NdTiO_{2+x}N_{1-x}$ powder was assembled into a thin film on precleaned conductive fluorine-doped tin oxide (FTO) glass (2.2 mm thick, Sigma-Aldrich) via an electrophoretic deposition (EPD) process. Concisely, 20 mg of $NdTiO_{2+x}N_{1-x}$ was dispersed in 30 mL of acetone containing 10 mg of iodine by 20 min sonication to obtain a uniform suspension. Two FTO slides were immersed into the suspension parallelly with an ∼10 mm gap, and then a 35 V bias was applied between them for 1 min. The FTO/$NdTiO_{2+x}N_{1-x}$ photoanodes were dried naturally in air.

A $NbCl_5$ impregnation step, which was adapted from $TaCl_5$ and $TiCl_4$,[15,23] was performed to improve the connection of particles. The FTO/$NdTiO_{2+x}N_{1-x}$ photoelectrode was soaked in 0.1 M $NbCl_5$ (99.99 wt %, abcr GmbH) dissolved in ethanol for 10 s and dried on a hot plate at 423 K. After repeating this procedure for four rounds, the electrode was then annealed in air at 573 K for 1 h to obtain FTO/$NdTiO_{2+x}N_{1-x}$/Nb_2O_5. The electrode was further decorated with a water oxidation cocatalyst, i.e., CoO_x. A 45 μL aliquot of 7 mM $Co(NO_3)_2$ dissolved in methanol was dropped on the FTO/$NdTiO_{2+x}N_{1-x}$/Nb_2O_5 surface followed by annealing at 473 K for 1 h. The composite electrode was washed with distilled water.

Characterization. Powder X-ray diffraction (PXRD) patterns were recorded in the transmission mode on a STOE STADI-P diffractometer (Cu Kα_1 radiation) equipped with a DECTRIS Mythen 1K detector. A UV−vis spectrophotometer (UV-2600, Shimadzu) was employed to characterize the optical properties with $BaSO_4$ as the reference. The IR spectra were acquired via a Nicolet Avatar 369 FT-IR spectrometer (Thermo Fisher Scientific, USA) with KBr as the reference. Scanning electron microscopy (SEM) images were collected via a Leo Supra 35VP SMT (Zeiss). High-angle annular dark-field (HAADF) images were collected on a JEOL-2100F in scanning transmission electron microscopy (STEM) mode. X-ray photoelectron spectroscopy (XPS) measurements were performed in a Prevac photoelectron spectrometer, an essential part of which was a hemispherical analyzer (VG SCIENTA R3000). The spectra were collected by using a monochromatized aluminum source Al Kα (E = 1486.6 eV) with no charge compensation. The C 1s reference peak at 285.0 eV (typical of C−C bonds) was used for calibration of the binding energy scale. The composition and chemical state were determined by analysis of areas and binding energies of Nd 3d, Nd 4d, Nb 3d, Co 2p, Ti 2p, O 1s, N 1s, and C 1s photoelectron peaks. All operations on the experimental data, including fitting the Shirley background and deconvolution with the mixed function of Gauss and Lorentz (GL = 30), were performed in the Casa XPS software.

Solid-State NMR Spectroscopy. The solid-state ^{1}H magic angle spinning (MAS) NMR spectrum was acquired at a magnetic field strength of 14.1 T (Larmor frequency 600.1 MHz) with a Bruker Avance III spectrometer equipped with a 1.3 mm MAS probehead and employing a MAS rate of 60.00 kHz. Acquisition involved a rotor-synchronized, double-adiabatic spin-echo sequence with a 90° excitation pulse of 1.1 μs, followed by two 50.0 μs tanh/tan short high-power adiabatic pulses with a 5 MHz frequency sweep.[24,25] All pulses operated at a nutation frequency of 210 kHz. A total of 256 signal transients with 5 s relaxation delay were accumulated. ^{1}H shifts were referenced by using neat tetramethylsilane (TMS).

Computational Methods. First-principles DFT calculations were performed by using the Vienna ab initio simulation package (VASP).[26−29] Projector-augmented-wave (PAW)[30] potentials with the exchange-correlation functional of Perdew−Burke−Ernzerhof (PBE)[31] were adopted. Semicore states were included, yielding the valence shells of $5s^26s^25p^65d^1$, $3s^23p^64s^13d^3$, $2s^22p^3$, and $2s^22p^4$ for Nd, Ti, N, and O, respectively. Note that the 4f electrons in Nd are treated as core electrons instead of valence electrons. The plane-wave energy cutoff was set to 600 eV. Meta-generalized gradient approximations (meta-GGA) with the new SCAN functional[32] were used in structural relaxations with a Γ-centered Monkhorst−Pack 6 × 4 × 6 k-mesh. Full ion optimizations are obtained with a threshold of self-consistent energy difference less than 10^{-6} eV and all forces smaller than 10^{-3} eV/Å^2. In addition, the hybrid HSE06 functional[33] was further used to obtain a more accurate band structure based on optimized structures that were obtained with the SCAN functional. In the density of states calculation, a denser 8 × 8 × 8 k-mesh was adopted.

https://dx.doi.org/10.1021/acs.inorgchem.0c03041
Inorg. Chem. 2021, 60, 919−929

Electrochemical Measurements. A conventional three-electrode setup was used to perform all the electrochemical measurements in 1 M NaOH electrolyte (pH = 13.6). The FTO slide deposited with $NdTiO_{2+x}N_{1-x}$ was used as a working electrode with an exposed geometrical surface area of ca. 0.79 cm^2. Platinum wire and a 1 M Ag/AgCl electrode were used as counter and reference electrodes, respectively. The recorded potential vs 1 M Ag/AgCl was converted subsequently vs RHE according to the Nernst equation $E_{RHE} = E^{\theta}_{1\,M\,Ag/AgCl} + 0.059\ V \times pH + E_{Ag/AgCl}$. The light source was 1 sun simulated solar irradiation (AM 1.5G, 100 mW cm^{-2}) generated by a solar light simulator (class-AAA 94023A, Newport) with an ozone-free 450 W xenon short-arc lamp. Mott−Schottky measurements were conducted by using the Gamry INTERFACE 1010T potentiostat/galvanostat/ZRA workstation at an ac amplitude of 5 mV and different frequencies under dark conditions. Electrochemical impedance spectroscopy (EIS) was measured at 1.0 V vs RHE in an ac potential frequency range of 20 kHz−0.2 Hz under an AM 1.5G illumination. The linear square voltammetry (LSV) curves were swept negatively at a scan rate of 10 mV s^{-1}, and chronoamperometry (CA) curves at a constant bias 1.23 V vs RHE were recorded with a potentiostat (PalmSens4, PalmSens BV). Open-circuit photovoltages (OCPV) were collected under chopped illumination.

RESULTS AND DISCUSSION

Structural Analysis. The topotactic transformation of oxides via nitridation has been frequently used toward the synthesis of metal oxynitrides, which can enhance the exploitation range of visible light.[35] The PXRD patterns of $Nd_2Ti_2O_7$ (Figure 1a) are characteristic of a material belonging to the family of compounds with a noncentrosymmetric structure having perovskite-type slabs (space group $P112_1$).[36] During ammonolysis at high temperature, the $Nd_2Ti_2O_7$ precursor was converted to an oxynitride through O^{2-}/N^{3-} substitution (Figure 1b). The resulting compound from the ammonolysis was identified as $NdTiO_{2+x}N_{1-x}$ by means of PXRD, matching with the previous report ICSD 94764 (Figure 1a).[36] The product crystallizes in a distorted perovskite-related structure (space group *Pnma*).[34]

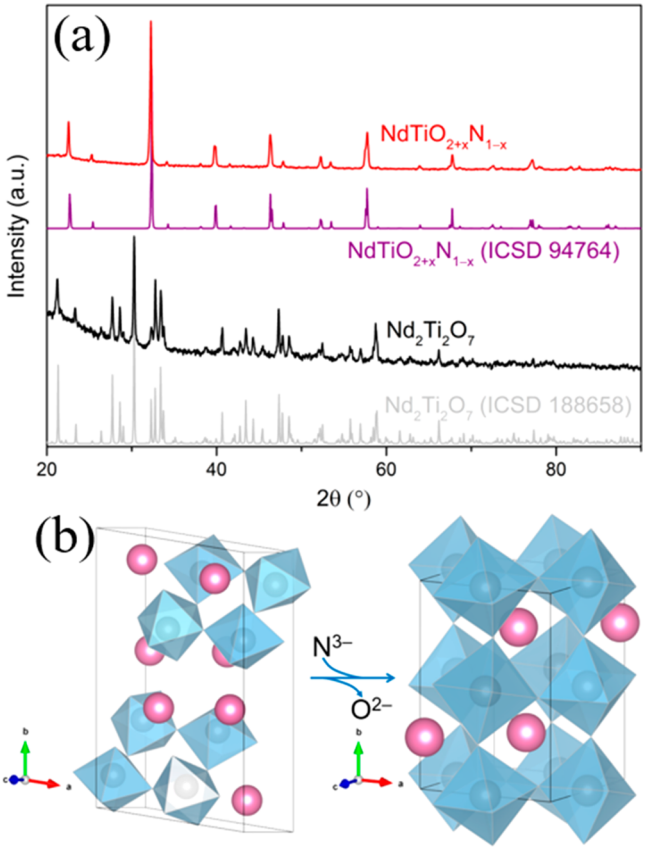

Figure 1. (a) PXRD pattern of $Nd_2Ti_2O_7$ and $NdTiO_{2+x}N_{1-x}$; for reference, the corresponding simulated PXRD patterns are also shown. (b) Crystal structural evolution from $Nd_2Ti_2O_7$ to $NdTiO_{2+x}N_{1-x}$ through O^{2-}/N^{3-} substitution. It should be mentioned that the composition of the ternary metal oxynitride has been previously reported to have an oxygen-rich composition $NdTiO_{2.17}N_{0.83}$, with a statistic O/N distribution (*vide infra*).[34]

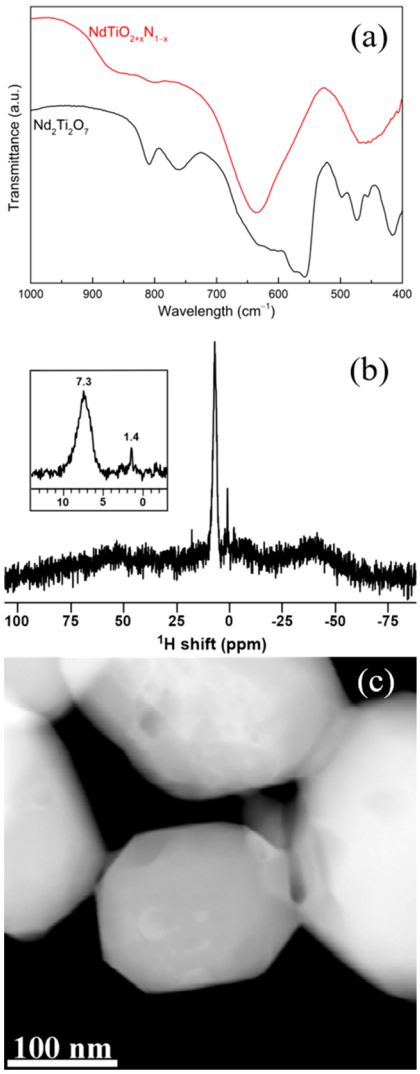

Figure 2. (a) IR spectra of $Nd_2Ti_2O_7$ and $NdTiO_{2+x}N_{1-x}$. (b) ^1H MAS NMR spectra of $NdTiO_{2+x}N_{1-x}$. The inset shows the zoomed ^1H NMR signal from $NdTiO_{2+x}N_{1-x}$. (c) HAADF image of $NdTiO_{2+x}N_{1-x}$ particles.

After chemical conversion from $Nd_2Ti_2O_7$ to $NdTiO_{2+x}N_{1-x}$ through O^{2-}/N^{3-} substitution, IR spectra have also been conducted to identify the bonding situation. As displayed in Figure 2a, the oxide precursor $Nd_2Ti_2O_7$ shows a typical spectral shape of lanthanide titanates $Ln_2Ti_2O_7$.[37,38] The broader peaks for the oxynitride $NdTiO_{2+x}N_{1-x}$ sample suggest high O/N disorder in the $TiO_{6-x}N_x$ octahedra.[34]

In Figure 2b the ^1H MAS NMR spectrum of $NdTiO_{2+x}N_{1-x}$ surface is shown. The proton signals are severely affected by paramagnetic interactions with unpaired electrons of the Nd^{3+}

https://dx.doi.org/10.1021/acs.inorgchem.0c03041
Inorg. Chem. 2021, 60, 919−929

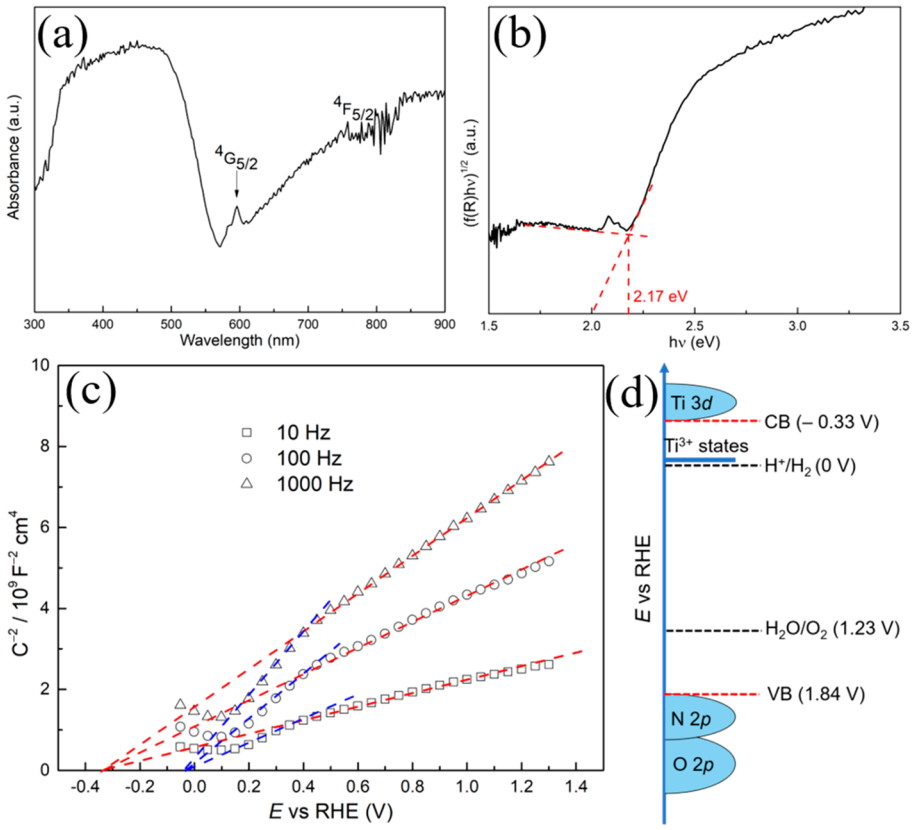

Figure 3. UV−vis diffuse reflectance spectra of $NdTiO_{2+x}N_{1-x}$ (a) and the corresponding Tauc plot (b). (c) Mott−Schottky plots for the FTO/$NdTiO_{2+x}N_{1-x}$ electrode recorded at various frequencies in 1 M NaOH electrolyte (pH 13.6) under dark conditions. (d) Band structure diagram of $NdTiO_{2+x}N_{1-x}$ including Ti^{3+} states.

ions. Most of the expected signal intensity is buried in the baseline as a broad, featureless bump. Only two narrow (albeit very weak) signals remain: at 7.3 and 1.4 ppm, which we assign to physisorbed water and hydroxyl groups, respectively. The general appearance of the spectrum is very similar to that collected from $CeTiO_2N$.[39] Importantly, in contrast to $CeTiO_2N$, the ^{14}N NMR signal from $NdTiO_{2+x}N_{1-x}$ could not be detected, which we attribute to the fact that $NdTiO_{2+x}N_{1-x}$ has a statistic O/N distribution over the anionic sites. This is in agreement with a previous report of Rosseinsky et al., who determined this deviation from the ordered structure $NdTiO_2N$ to be the slightly oxygen-rich $NdTiO_{2.2}N_{0.8}$ with negligible O/N ordering.[34] Because the O/N ratio may be modified under the anodic PEC operation, resulting from noncomplete surface passivation, we chose to denote to the title compound for the sake of clarity as $NdTiO_{2+x}N_{1-x}$. The successful incorporation of nitrogen has been proved by complementary experimental analysis (*vide infra*). Therefore, the unusually high local symmetry of nitrogen environments in these systems is not fully satisfied in $NdTiO_{2+x}N_{1-x}$.[39] The HAADF image reveals the particle size of $NdTiO_{2+x}N_{1-x}$ to be ∼150 nm in diameter with regular shapes (Figure 2c).

Experimental Electronic Structure. UV−vis diffuse reflectance spectra depicted in Figure 3a were used to analyze the optical property of $NdTiO_{2+x}N_{1-x}$. A clear absorption edge at ∼610 nm was confirmed, which is characteristic for $NdTiO_{2+x}N_{1-x}$. The background absorption (tail) in the infrared region indicates the presence of Ti^{3+} species originating from the partial reduction of Ti^{4+}.[22,40] However, it is not possible to determine, based on the IR analysis, the quantitative Ti^{3+}/Ti^{4+} ratio. The phenomenon is more common occurring for niobium- and titanium-based oxynitrides than for tantalum-based oxynitrides because of the higher chemical stability of Ta^{5+} compared to that of Nb^{5+} and Ti^{4+}.[22,41−43] Another weak feature with respect to $^4G_{5/2}$ and $^4F_{5/2}$ f−f transitions on Nd^{3+} was also observed. The E_g was determined to be 2.17 eV by the Tauc plot derived (Figure 3b) from the UV−vis spectra, close to the previously reported value 2.1 eV for $NdTiO_{2+x}N_{1-x}$.[22]

It is generally known that the flat band potential (V_f) can be estimated via the Mott−Schottky equation:[44]

$$\frac{1}{C^2} = \frac{2}{e_0 \varepsilon \varepsilon_0 N_d}\left(V - V_f - \frac{k_B T}{e_0}\right) \quad (1)$$

where C is the interfacial capacitance, N_d the number of donors, V the applied voltage, e_0 the electronic charge, ε the dielectric constant of the semiconductor, ε_0 the permittivity of free space, k_B Boltzmann's constant, and T the absolute temperature. Therefore, the potential V_f can be obtained by extrapolation of the linear portion to the x-axis intercept from the plot of (differential capacitance)$^{-2}$ against the electrode potential. The Mott−Schottky plots measured at 10, 100, and 1000 Hz are presented in Figure 3c. The sample developed positive slopes in plots as expected for n-type semiconductors. The capacitances were found to be frequency-dependent, revealing Fermi level pinning due to a midgap state.[45] The V_f was determined to be −0.33 V vs RHE from Figure 3c, which is very close to $LaTiO_2N$ at −0.37 vs RHE.[46] It is interesting to

https://dx.doi.org/10.1021/acs.inorgchem.0c03041
Inorg. Chem. 2021, 60, 919−929

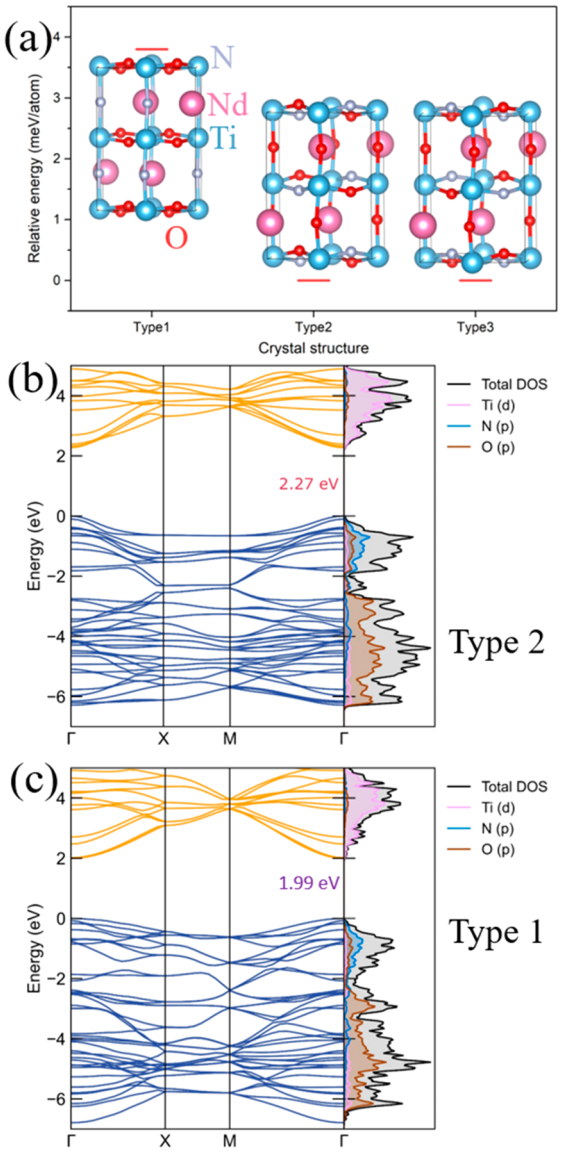

Figure 4. (a) Three simulated structures for model $NdTiO_2N$ composition, with different kinds of N/O distributions. The energies are relative to type 2, the one that possesses the lowest energy. Type 2 is used for further electronic structure calculation. (b) Electronic band structure and projected density of states using the HSE06 functional. The Fermi level is set to zero. The electronic band gap is calculated to be 2.27 eV. (c) Electronic band structure and projected density of states with type 1 configuration.

note that secondary linearity portions (blue dashed lines) in the plots can be seen. In connection with the UV−vis absorption discussion, the secondary linearity portions were likely caused by shallow Ti^{3+} defects near the conduction band.[40,47−50] The sub-band originated from shallow Ti^{3+} states and was estimated to be centered at −0.03 V vs RHE, slightly above the reduction potential of water. In combination with the UV−vis analysis, the positions of both CB minimum and VB maximum are therefore located approximately at −0.33 V vs RHE and 1.84 V vs RHE, respectively. The band structure diagram of $NdTiO_2N$ including Ti^{3+} states is depicted in Figure 3d, together with the reduction and oxidation potentials of water. The band positions of $NdTiO_{2+x}N_{1-x}$ make it theoretically suitable for overall water splitting on a single absorber.

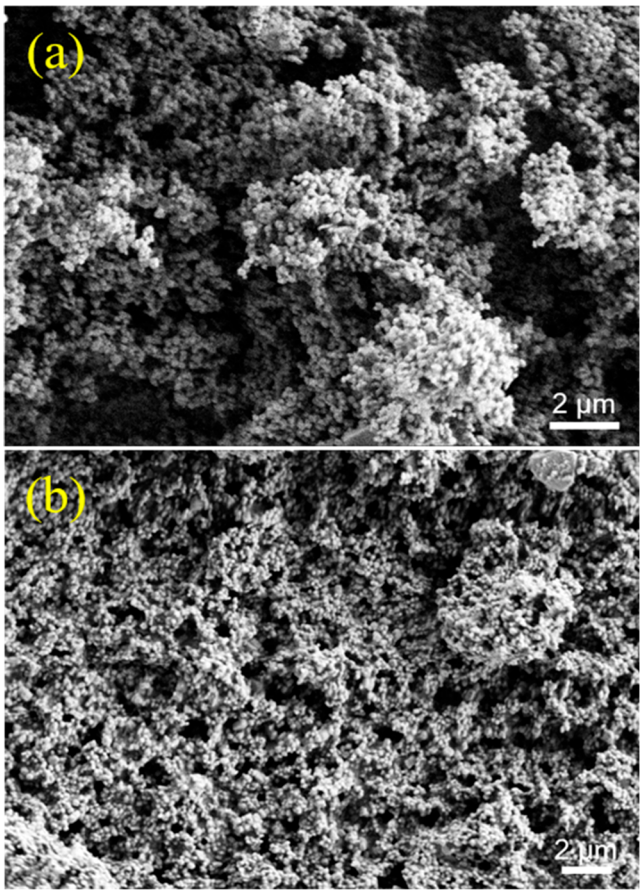

Figure 5. SEM images of FTO/$NdTiO_{2+x}N_{1-x}$ photoanodes (a) before and (b) after Nb_2O_5 and CoO_x postmodification.

Calculated Electronic Structure. As the counterpart of experimental analysis, we performed theoretical investigations at the DFT level to elaborate more details of the electronic structure for the title compound. Three crystal structures with the same chemical compositions, but different N/O distributions, were first created (Figure 4a), and the corresponding lattice parameters and volumetric data are presented in Table S1. Thermodynamically, the one that possesses the lowest energy is much more likely to approach the experimental structure (type 2, two nitrogen atoms in a *cis*-type configuration) given thermodynamical control. The structure configuration was therefore used for further electronic structure calculation. The electronic band structure was calculated along the high-symmetry path "Γ(0, 0, 0) − $X(^1/_2, 0, 0)$ − $M(^1/_2, ^1/_2, 0)$ − Γ(0, 0, 0)". The results produced by using the SCAN and HSE06 functionals are depicted in Figure S1 and Figure 4b, respectively, in combination with its density of states (DOS).[51] Note that because of the strong correlation for Nd 4f electrons, large self-interaction error occurs when these 4f electrons are treated as valence electrons. Indeed, it falsely describes the $NdTiO_2N$ as metallic, while experiments confirm it to be semiconducting.[52] Therefore, we used a pseudopotential that treats the 4f electrons (orbitals) as core, accounting for their strong contraction. A direct band gap of 1.36 eV at the Γ point was obtained with SCAN, which is smaller than the experimental value 2.17 eV. After having included the Hartree−Fock exact exchange contribution (HSE06),[53] it leads to a wider band gap of 2.27 eV, in good agreement with the estimated experimental

https://dx.doi.org/10.1021/acs.inorgchem.0c03041
Inorg. Chem. 2021, 60, 919−929

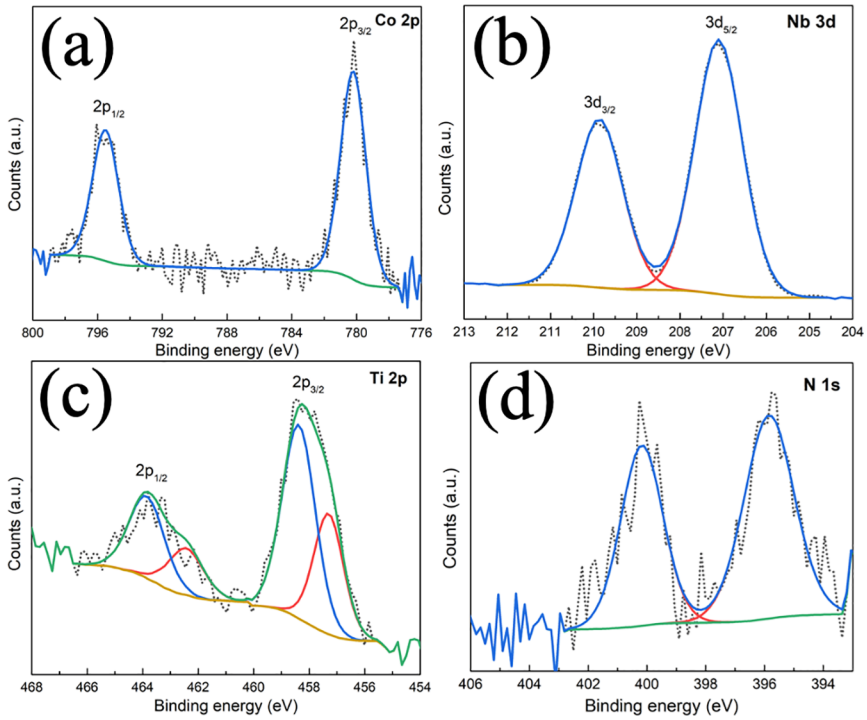

Figure 6. XPS analysis on Co 2p (a), Nb 3d (b), Ti 2p (c), and N 1s (d) spectra of the FTO/$NdTiO_{2+x}N_{1-x}$/Nb_2O_5/CoO_x electrode.

result. The additional calculation on the type 1 configuration, in which the N and O atoms have different local positions with type 2 structure, yielded a band gap value of 1.99 eV (Figure 4c), consistent with previous reports.[19] From its projected density of states (DOS), one can also observe that the valence bands are predominantly of N 2p and O 2p character, while the conduction bands are of Ti 3d character.

Characterization of Photoanodes. Figure 5a shows the SEM image of $NdTiO_{2+x}N_{1-x}$ particles assembled as thin films on FTO. $NdTiO_{2+x}N_{1-x}$ particles were estimated to be around 200 nm in diameter with irregular shapes. After postnecking with Nb_2O_5 and CoO_x overlayers, the particles were maintained in the original shapes (Figure 5b).

The XPS technique was employed to analyze the surface composition of the as-prepared composite FTO/$NdTiO_{2+x}N_{1-x}$/Nb_2O_5/CoO_x electrode. The collected spectra of the active phases (Co 2p, Nb 3d, Ti 2p, N 1s, and Nd 4d) are presented in Figure 6 and Figure S2. Analyzing the structure of the electrode from outermost layers introduced by the subsequent covering FTO substrate, we find a cobalt phase with a chemical nature revealed by the XPS Co 2p spectrum (Figure 6a). The characteristic doublet of Co $2p_{3/2}$ (780.2 eV) and Co $2p_{1/2}$ (795.5 eV) with spin−orbit splitting of 15.3 eV and no clear satellite structure confirms the presence of OER cocatalyst CoO_x with the dominant role of low-spin Co^{3+}.[54] In turn, in the XPS Nb 3d spectrum the positions of the spin−orbit $3d_{5/2}$ (207.1 eV) and $3d_{3/2}$ (209.9 eV) components as well as symmetric peak shapes indicate the formation of a Nb_2O_5 phase (Figure 6b) which can related to the photoabsorber particles.[55] The core component of the studied semiconducting material is $NdTiO_{2+x}N_{1-x}$, and the elements were analyzed on the basis of the XPS Ti 2p, N 1s, and Nd 4d spectra (Figure 6c,d and Figure S2). The full width at half-maximum (FWHM) of the Ti $2p_{3/2}$ and Ti $2p_{1/2}$ peaks is high enough to suggest the presence of Ti in various chemical environments. This is understandable due to the incorporation of Ti^{4+} into the $NdTiO_{2+x}N_{1-x}$ oxynitride structure. The Ti $2p_{3/2}$ photoemission at 458.4 eV (with corresponding the Ti $2p_{1/2}$ component at 463.9 eV) is attributed to Ti in Ti−O bonds, while that at 457.3 eV (Ti $2p_{1/2}$ at 462.4 eV) is assigned to Ti in N−Ti−O bonds.[56] These result suggest Ti^{4+} cations locating in $TiO_{6-x}N_x$ octahedra. Two peaks of N 1 spectra located at 395.8 and 400.1 eV were observed (Figure 6d); similar pair peaks have been reported for N-doped TiO_2 and (La, Sr)TiO_2N.[57,58] The peak at binding energy of 395.8 eV indicates the incorporation of N into the metal oxynitride lattice. The peak at the higher binding energy of 400.1 eV can be attributed to either chemisorbed molecular N_2 on the surface or atomic β-N of TiN.[57,58] The exact interpretation of the Nd 3d region is troublesome due to the overlapping O KLL peaks. Therefore, we decided to use the less frequently analyzed, but more easily interpreted, Nd 4d spectrum. The Nd $4d_{5/2}$ photoemission observed at 121.9 eV clearly confirms neodymium presents in Nd^{3+} state (Figure S2).[59,60]

Evaluation of Photoelectrochemical Properties. Although $NdTiO_{2+x}N_{1-x}$ has the capability of absorbing a wide range of visible light, the photoelectrode fabricated by means of EPD offered negligible photoresponse upon chopped irradiation (Figure 7a). The low PEC performance of EPD-based photoelectrodes has been ascribed to the weak adhesion to the substrate and low interparticular electric conductivity.[43,61] A postnecking treatment step was thus applied to the as-prepared particle-based $NdTiO_{2+x}N_{1-x}$ thin film by hydrolysis of the $NbCl_5$−ethanol solution, forming a thin Nb_2O_5 networking layer. As a consequence, the modified FTO/$NdTiO_{2+x}N_{1-x}$/Nb_2O_5 electrode yielded noticeable anodic photocurrent compared to the as-deposited FTO/$NdTiO_{2+x}N_{1-x}$ photoelectrode. It should be mentioned that similar effects have been observed on $Pb_2Ti_4O_9F_2$, $Pb_2Ti_2O_{5.4}F_{1.2}$, and TaON particle-based thin film photoanode by modifying with Ta_2O_5 or TiO_2 driving from $TaCl_5$ or $TiCl_4$.[15,23,62]

https://dx.doi.org/10.1021/acs.inorgchem.0c03041
Inorg. Chem. 2021, 60, 919−929

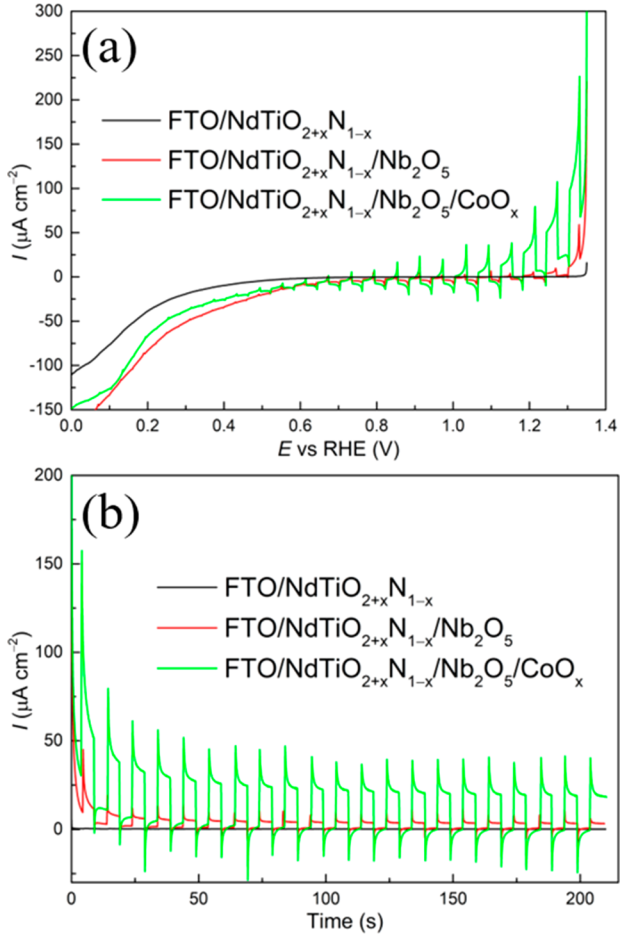

Figure 7. (a) LSV curves of FTO/$NdTiO_{2+x}N_{1-x}$ photoanode and the ones with sequentially Nb_2O_5 and CoO_x overlayers at a scan rate of 10 mV s^{-1}. (b) CA curves of FTO/$NdTiO_{2+x}N_{1-x}$ photoanode and the ones with sequential Nb_2O_5 and CoO_x overlayers at a constant potential of 1.23 V vs RHE. Measurements were performed in 1 M NaOH electrolyte (pH 13.6) under interrupted AM 1.5G illumination (100 mW cm^{-2}).

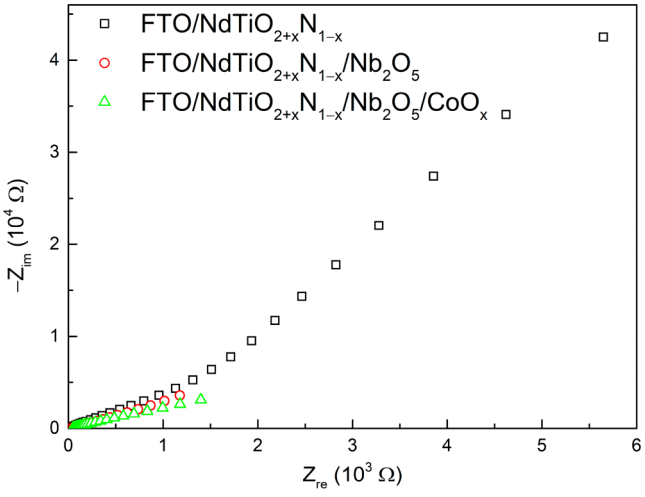

Figure 8. Nyquist plots for FTO/$NdTiO_{2+x}N_{1-x}$ photoanodes before and after modification with Nb_2O_5 and CoO_x measured at 1.0 V vs RHE under AM 1.5G illumination and at the frequency range 20 kHz−0.2 Hz.

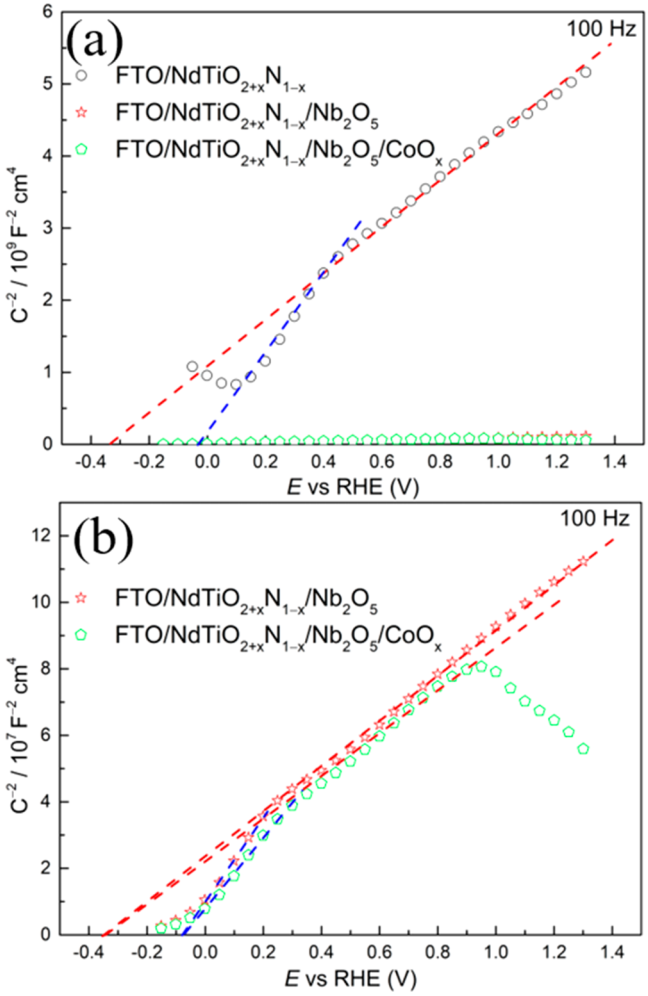

Figure 9. (a) Mott−Schottky plots for the FTO/$NdTiO_{2+x}N_{1-x}$ photoanode and the ones with sequential Nb_2O_5 and CoO_x overlayers recorded at 100 Hz in 1 M NaOH electrolyte (pH 13.6) under dark conditions. (b) Magnification of the same plot (note the different *y*-axis).

Because bare n-type semiconducting photoanodes tend to suffer from poor surface water oxidation kinetics,[63,64] the photoexcited holes could thus accumulate at the surface and lead to photocorrosion.[65,66] The photocurrent density of the FTO/$NdTiO_{2+x}N_{1-x}$/Nb_2O_5 photoanode in conjunction with a known OER cocatalyst, i.e., CoO_x, was compared and presented in Figure 7a. The photocurrent was improved considerably because of enhanced reaction kinetics and efficient utilization of the photogenerated holes reaching the electrode surface for water oxidation,[67] and a final photocurrent density of ca. 60 μA cm^{-2} was developed at 1.23 V vs RHE. The photoresponse begins at very negative onset potential close to 0 V vs RHE (Figure S3, enlarged range between 0 and 0.4 V vs RHE of Figure 7a), profiting from its negative flat band potential. The postamelioration effect of Nb_2O_5 and CoO_x overlayers was also reflected in the CA curves measured at constant potential of 1.23 V vs RHE (Figure 7b). Both the LSV and CA curves exhibit obvious spikes caused by processes at the semiconductor surface upon switching illumination.[68,69]

Mechanism of Activation. Besides the direct evidence provided by SEM in Figure 5, additional electrochemical analytic techniques were performed to reveal the reasons of the

https://dx.doi.org/10.1021/acs.inorgchem.0c03041
Inorg. Chem. 2021, 60, 919−929

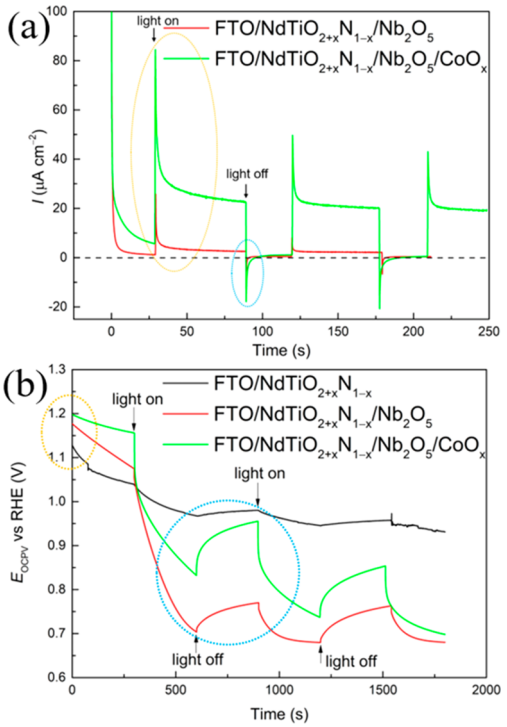

Figure 10. (a) Transient photocurrent (TPC) measurements for the photoanode of $FTO/NdTiO_{2+x}N_{1-x}/Nb_2O_5$ and $FTO/NdTiO_{2+x}N_{1-x}/Nb_2O_5$ in 1 M NaOH electrolyte and (b) OCPV curves measured with for the $FTO/NdTiO_{2+x}N_{1-x}$ photoanode and the ones with sequential Nb_2O_5 and CoO_x overlayers in 1 M NaOH electrolyte without hole scavenger.

enhanced PEC performance induced by postmodification. EIS measurements were performed to evaluate the electrical properties of $NdTiO_{2+x}N_{1-x}$ photoanode before and after modification with Nb_2O_5 and CoO_x. As presented in Figure 8, the Nb_2O_5-modified $FTO/NdTiO_{2+x}N_{1-x}$ photoanode exhibited a much diminished arc radius of the semicircular Nyquist plot, evidencing that the thin Nb_2O_5 network and the altered adhesion could reduce the charge transfer resistance. The charge transport properties were further ameliorated when decorating with a OER cocatalyst CoO_x (Figure 8). The CoO_x decoration was supposed to accelerate the utilization of surface photogenerated holes to oxidize water, concurrently inducing extraction of deep charge carriers.[70] Thus, improvement PEC performance was achieved in Figure 7.

Comparative analysis of Mott−Schottky plots was conducted on the modified $FTO/NdTiO_{2+x}N_{1-x}$ photoanode. The flat band potential related to band bending was negatively shifted slightly as shown in Figure 9, indicating enlarged band bending at the electrode/electrolyte interface which facilitates charge separation and transfer. The charge recombination at the interface can be suppressed because of negative flat band potential blocking electrons.[71] Other illustrious features of these Mott−Schottky plots are the decreasing slopes after posttreatment. The donor concentration N_d is inversely proportional to the Mott−Schottky plot slope according to eq 2:[45]

$$N_d = \frac{2}{e_0 \varepsilon \varepsilon_0}\left[\mathrm{d}\left(\frac{1}{c^2}\right)\Big/\mathrm{d}V\right]^{-1} \quad (2)$$

Though the qualitative N_d cannot be obtained due to the unknown dielectric constant ε of $NdTiO_{2+x}N_{1-x}$, the N_d was strongly increased by means of Nb_2O_5 treatment. The augmented value of N_d awakened the $FTO/NdTiO_{2+x}N_{1-x}$ from negligible photoresponse (Figure 7). A cocatalyst CoO_x modification raised the N_d slightly further, but the photocurrent was significantly advanced. These were ascribed to prolonged lifetime and boosted charge separation.

To probe the CoO_x effect in more detail, complementary transient photocurrent (TPC) measurements were performed and are depicted in Figure 10a. After deposition of the CoO_x cocatalyst, the greater initial anodic photocurrent spike, which originated from separation of photogenerated electron−hole pairs at the electrode/electrolyte interface,[72] indicated that holes can be captured by the new active sites for water oxidation. The $FTO/NdTiO_{2+x}N_{1-x}/Nb_2O_5/CoO_x$ photoanode also had a remarkably longer photocurrent decay time than that of $FTO/NdTiO_{2+x}N_{1-x}/Nb_2O_5$, which can be attributed to the efficient separation and transfer of photogenerated charges. A cathodic current peak was observed upon turning off the light, and the current was restored to the initial dark level. The higher amount of cathodic charge was consistent with the longer photocurrent decay time.[73] The quantitative decay times were calculated to be 0.34 and 1.27 s (Figure S4) for $FTO/NdTiO_{2+x}N_{1-x}/Nb_2O_5$ and $FTO/NdTiO_{2+x}N_{1-x}/Nb_2O_5/CoO_x$, respectively. The CoO_x modification results in longer lifetime of the charge carrier.

Because surface states could lead to Fermi level pinning at the surface,[74] ideal photoanodes with no Fermi level pinning would expect to produce an open circuit potential under dark conditions (OCP_{dark}) close to 1.23 V vs RHE.[75] As marked with orange oval in Figure 10b, the OCP_{dark} of bare $FTO/NdTiO_{2+x}N_{1-x}$ positively shifted from 1.12 to 1.18 V vs RHE due to altered surface trap states by necking with the Nb_2O_5 thin overlayer. Grafting the OER catalyst CoO_x diminished the Fermi level pinning effect further; thus, the equilibrium potential OCP_{dark} was pressed toward the water oxidation potential.[73] For photoelectrodes, the difference between open circuit potential in dark and light, i.e., OCPV, is crucial. Incremental OCPV with sequentially Nb_2O_5 and CoO_x overlayers was observed in Figure 10b (blue circle), which is equal to a higher driving force toward water oxidation and therewith enhanced photocurrent (Figure 7).[76,77]

CONCLUSIONS

In summary, the properties of one member of the titanium-based quaternary oxynitrides, i.e., $NdTiO_{2+x}N_{1-x}$, were investigated. The band gap of the mixed-anion compound $NdTiO_{2+x}N_{1-x}$ was determined to be 2.17 eV, only slightly different from the theoretical value calculated at the DFT level. Mott−Schottky measurements demonstrate that $NdTiO_{2+x}N_{1-x}$ possesses a relative negative CB edge located at around −0.33 vs RHE, more negative than the potential of water reduction. The VB edge was thus proposed to be 1.84 V vs RHE, indicating a band structure beyond the reduction and oxidation potentials of water. This makes the title compound theoretically able to perform overall water splitting on a single absorber. Furthermore, the solid-state ^{14}N NMR signals of $NdTiO_{2+x}N_{1-x}$ could not be detected, confirming that $NdTiO_{2+x}N_{1-x}$ is not exactly stoichiometric in comparison to structurally related metal oxynitrides.

Examining the particle-based bare photoanode did not exhibit noticeable photocurrent. Exceptionally, a noteworthy augmented photocurrent was achieved after subjecting to postdeposition of Nb_2O_5 and CoO_x overlayer. SEM, EIS, and

https://dx.doi.org/10.1021/acs.inorgchem.0c03041
Inorg. Chem. 2021, 60, 919−929

Mott−Schottky analysis evidenced that the thin Nb_2O_5 overlayer could enhance the connections between the $NdTiO_{2+x}N_{1-x}$ particles and thus increased the charge carrier concentration, significantly facilitating charge transfer. OCPV and TPC measurements confirmed that the OER cocatalyst CoO_x overlayer can ameliorate the surface states and accelerate the utilization of surface photogenerated holes, therefore extracting deeper holes and prolonging their lifetime. Our results highlight the capability of $NdTiO_{2+x}N_{1-x}$ as photoactive material with a wide visible light absorption edge for PEC water splitting. Further efforts on synthesis of nanoscopic forms of the title compounds should improve the PEC efficiency by decoupling charge carrier transport from light absorption.

■ ASSOCIATED CONTENT

Supporting Information

The Supporting Information is available free of charge at https://pubs.acs.org/doi/10.1021/acs.inorgchem.0c03041.

Lattice parameters and volumetric data for the studied $NdTiO_{2+x}N_{1-x}$ systems; the electronic band structure and projected density of states using SCAN functional; XPS analysis on Nd 4d spectra of the FTO/$NdTiO_{2+x}N_{1-x}$/Nb_2O_5/CoO_x electrode; the enlarged range between 0 and 0.4 V vs RHE in Figure 7; calculation of transient decay time (PDF)

■ AUTHOR INFORMATION

Corresponding Authors

Adam Slabon − *Department of Materials and Environmental Chemistry, Stockholm University, 106 91 Stockholm, Sweden;* orcid.org/0000-0002-4452-1831; Email: adam.slabon@mmk.su.se

Zili Ma − *Institute of Inorganic Chemistry, RWTH Aachen University, 52056 Aachen, Germany;* orcid.org/0000-0001-7975-9201; Email: zili.ma@ac.rwth-aachen.de

Authors

Kaixuan Chen − *Institute of Inorganic Chemistry, RWTH Aachen University, 52056 Aachen, Germany;* orcid.org/0000-0002-7864-7440

Aleksander Jaworski − *Department of Materials and Environmental Chemistry, Stockholm University, 106 91 Stockholm, Sweden;* orcid.org/0000-0002-7156-559X

Jianhong Chen − *Department of Materials and Environmental Chemistry, Stockholm University, 106 91 Stockholm, Sweden*

Anna Rokicińska − *Faculty of Chemistry, Jagiellonian University, 30-387 Kraków, Poland*

Piotr Kuśtrowski − *Faculty of Chemistry, Jagiellonian University, 30-387 Kraków, Poland;* orcid.org/0000-0001-8496-0559

Richard Dronskowski − *Institute of Inorganic Chemistry, RWTH Aachen University, 52056 Aachen, Germany; Hoffmann Institute of Advanced Materials, Shenzhen Polytechnic, Shenzhen 518055, China;* orcid.org/0000-0002-1925-9624

Complete contact information is available at: https://pubs.acs.org/10.1021/acs.inorgchem.0c03041

Author Contributions

Z.M. and K.C. contributed equally to this work.

Notes

The authors declare no competing financial interest.

■ ACKNOWLEDGMENTS

A.S. thanks Vinnova, the Swedish innovation agency, for financial support (project: C1Bio 2019-03174). We thank Xianji Qiao for helpful discussions and Birgit Hahn for SEM measurements. Z.M. thanks the China Scholarship Council for a Ph.D. scholarship. K.C. gratefully thanks the financial support from the Alexander von Humboldt Foundation. The XPS measurements were performed with the equipment purchased with the financial support of the European Regional Development Fund in the framework of the Polish Innovation Operational Program (Contract POIG.02.01.00-12-023/08). The simulation work was supported by the IT center of RWTH Aachen University under Grant JARA-HPC (JARA0179).

■ REFERENCES

(1) Lu, C.; Ma, Z.; Jäger, J.; Budnyak, T. M.; Dronskowski, R.; Rokicińska, A.; Kuśtrowski, P.; Pammer, F.; Slabon, A. NiO/Poly(4-Alkylthiazole) Hybrid Interface for Promoting Spatial Charge Separation in Photoelectrochemical Water Reduction. *ACS Appl. Mater. Interfaces* **2020**, *12*, 29173−29180.

(2) Hogerwaard, J.; Dincer, I.; Naterer, G. F. Experimental Investigation and Optimization of Integrated Photovoltaic and Photoelectrochemical Hydrogen Generation. *Energy Convers. Manage.* **2020**, *207*, 112541.

(3) Volokh, M.; Peng, G.; Barrio, J.; Shalom, M. Carbon Nitride Materials for Water Splitting Photoelectrochemical Cells. *Angew. Chem., Int. Ed.* **2019**, *58*, 6138−6151.

(4) Sivula, K.; van de Krol, R. Semiconducting Materials for Photoelectrochemical Energy Conversion. *Nat. Rev. Mater.* **2016**, *1*, 15010.

(5) Kageyama, H.; Hayashi, K.; Maeda, K.; Attfield, J. P.; Hiroi, Z.; Rondinelli, J. M.; Poeppelmeier, K. R. Expanding Frontiers in Materials Chemistry and Physics with Multiple Anions. *Nat. Commun.* **2018**, *9*, 772.

(6) Chien, P.-H.; Harada, J. K.; Liu, H.; Patel, S.; Huang, C.; Rondinelli, J. M.; Poeppelmeier, K. R.; Hu, Y.-Y. Microscopic Insights into the Reconstructive Phase Transition of $KNaNbOF_5$ with ^{19}F NMR Spectroscopy. *Chem. Mater.* **2020**, *32*, 5715−5722.

(7) Dang, U.; Zaheer, W.; Zhou, W.; Kandel, A.; Orr, M.; Schwenz, R. W.; Laurita, G.; Banerjee, S.; Macaluso, R. T. Lattice Anharmonicity of Stereochemically Active Lone Pairs Controls Thermochromic Band Gap Reduction of $PbVO_3Cl$. *Chem. Mater.* **2020**, *32*, 7404−7412.

(8) Oró-Solé, J.; Fina, I.; Frontera, C.; Gàzquez, J.; Ritter, C.; Cunquero, M.; Loza-Alvarez, P.; Conejeros, S.; Alemany, P.; Canadell, E.; Fontcuberta, J.; Fuertes, A. Engineering Polar Oxynitrides: Hexagonal Perovskite $BaWON_2$. *Angew. Chem., Int. Ed.* **2020**, *59*, 18395−18399.

(9) Balaz, S.; Porter, S. H.; Woodward, P. M.; Brillson, L. J. Electronic Structure of Tantalum Oxynitride Perovskite Photocatalysts. *Chem. Mater.* **2013**, *25*, 3337−3343.

(10) Davi, M.; Drichel, A.; Mann, M.; Scholz, T.; Schrader, F.; Rokicinska, A.; Kustrowski, P.; Dronskowski, R.; Slabon, A. Enhanced Photoelectrochemical Water Oxidation Efficiency of $CuWO_4$ Photoanodes by Surface Modification with Ag_2NCN. *J. Phys. Chem. C* **2017**, *121*, 26265−26274.

(11) Chen, Z.; Löber, M.; Rokicińska, A.; Ma, Z.; Chen, J.; Kuśtrowski, P.; Meyer, H.-J.; Dronskowski, R.; Slabon, A. Increased Photocurrent of $CuWO_4$ Photoanodes by Modification with the Oxide Carbodiimide $Sn_2O(NCN)$. *Dalt. Trans.* **2020**, *49*, 3450−3456.

(12) Seo, J.; Hisatomi, T.; Nakabayashi, M.; Shibata, N.; Minegishi, T.; Katayama, M.; Domen, K. Efficient Solar-Driven Water Oxidation

over Perovskite-Type $BaNbO_2N$ Photoanodes Absorbing Visible Light up to 740 Nm. *Adv. Energy Mater.* **2018**, *8*, 1800094.
(13) Kubo, A.; Giorgi, G.; Yamashita, K. Anion Ordering in $CaTaO_2N$: Structural Impact on the Photocatalytic Activity. Insights from First-Principles. *Chem. Mater.* **2017**, *29*, 539−545.
(14) Pihosh, Y.; Nandal, V.; Minegishi, T.; Katayama, M.; Yamada, T.; Seki, K.; Sugiyama, M.; Domen, K. Development of a Core−Shell Heterojunction Ta_3N_5-Nanorods/$BaTaO_2N$ Photoanode for Solar Water Splitting. *ACS Energy Lett.* **2020**, *5*, 2492−2497.
(15) Hirayama, N.; Nakata, H.; Wakayama, H.; Nishioka, S.; Kanazawa, T.; Kamata, R.; Ebato, Y.; Kato, K.; Kumagai, H.; Yamakata, A.; Oka, K.; Maeda, K. Solar-Driven Photoelectrochemical Water Oxidation over an n-Type Lead−Titanium Oxyfluoride Anode. *J. Am. Chem. Soc.* **2019**, *141*, 17158−17165.
(16) Bai, Y.; Ye, L.; Chen, T.; Wang, L.; Shi, X.; Zhang, X.; Chen, D. Facet-Dependent Photocatalytic N_2 Fixation of Bismuth-Rich Bi_5O_7I Nanosheets. *ACS Appl. Mater. Interfaces* **2016**, *8*, 27661−27668.
(17) Yoshitomi, F.; Sekizawa, K.; Maeda, K.; Ishitani, O. Selective Formic Acid Production via CO_2 Reduction with Visible Light Using a Hybrid of a Perovskite Tantalum Oxynitride and a Binuclear Ruthenium(II) Complex. *ACS Appl. Mater. Interfaces* **2015**, *7*, 13092−13097.
(18) Ebbinghaus, S. G.; Abicht, H. P.; Dronskowski, R.; Müller, T.; Reller, A.; Weidenkaff, A. Perovskite-Related Oxynitrides-Recent Developments in Synthesis, Characterisation and Investigations of Physical Properties. *Prog. Solid State Chem.* **2009**, *37*, 173−205.
(19) Wolff, H.; Dronskowski, R. First-Principles and Molecular-Dynamics Study of Structure and Bonding in Perovskite-Type Oxynitrides ABO_2N (A = Ca, Sr, Ba; B = Ta, Nb). *J. Comput. Chem.* **2008**, *29*, 2260−2267.
(20) Chun, W.-J.; Ishikawa, A.; Fujisawa, H.; Takata, T.; Kondo, J. N.; Hara, M.; Kawai, M.; Matsumoto, Y.; Domen, K. Conduction and Valence Band Positions of Ta_2O_5, TaON, and Ta_3N_5 by UPS and Electrochemical Methods. *J. Phys. Chem. B* **2003**, *107*, 1798−1803.
(21) Akiyama, S.; Nakabayashi, M.; Shibata, N.; Minegishi, T.; Asakura, Y.; Abdulla-Al-Mamun, M.; Hisatomi, T.; Nishiyama, H.; Katayama, M.; Yamada, T.; Domen, K. Highly Efficient Water Oxidation Photoanode Made of Surface Modified $LaTiO_2N$ Particles. *Small* **2016**, *12*, 5468−5476.
(22) Porter, S. H.; Huang, Z.; Dou, S.; Brown-Xu, S.; Golam Sarwar, A. T. M.; Myers, R. C.; Woodward, P. M. Electronic Structure and Photocatalytic Water Oxidation Activity of R $TiNO_2$ (R = Ce, Pr, and Nd) Perovskite Nitride Oxides. *Chem. Mater.* **2015**, *27*, 2414−2420.
(23) Maeda, K.; Hirayama, N.; Nakata, H.; Wakayama, H.; Oka, K. Oxyfluoride $Pb_2Ti_4O_9F_2$ as a Stable Anode Material for Photoelectrochemical Water Oxidation. *J. Phys. Chem. C* **2020**, *124*, 1844−1850.
(24) Kervern, G.; Pintacuda, G.; Emsley, L. Fast Adiabatic Pulses for Solid-State NMR of Paramagnetic Systems. *Chem. Phys. Lett.* **2007**, *435*, 157−162.
(25) Hwang, T.; van Zijl, P. C. M.; Garwood, M. Fast Broadband Inversion by Adiabatic Pulses. *J. Magn. Reson.* **1998**, *133*, 200−203.
(26) Kresse, G.; Furthmüller, J. Efficient Iterative Schemes for Ab Initio Total-Energy Calculations Using a Plane-Wave Basis Set. *Phys. Rev. B: Condens. Matter Mater. Phys.* **1996**, *54*, 11169−11186.
(27) Kresse, G.; Hafner, J. Ab Initio Molecular Dynamics for Liquid Metals. *Phys. Rev. B: Condens. Matter Mater. Phys.* **1993**, *47*, 558−561.
(28) Kresse, G.; Furthmüller, J. Efficiency of Ab-Initio Total Energy Calculations for Metals and Semiconductors Using a Plane-Wave Basis Set. *Comput. Mater. Sci.* **1996**, *6*, 15−50.
(29) Kresse, G.; Hafner, J. Norm-Conserving and Ultrasoft Pseudopotentials for First-Row and Transition Elements. *J. Phys.: Condens. Matter* **1994**, *6*, 8245−8257.
(30) Kresse, G.; Joubert, D. From Ultrasoft Pseudopotentials to the Projector Augmented-Wave Method. *Phys. Rev. B: Condens. Matter Mater. Phys.* **1999**, *59*, 1758−1775.
(31) Perdew, J. P.; Burke, K.; Ernzerhof, M. Generalized Gradient Approximation Made Simple. *Phys. Rev. Lett.* **1996**, *77*, 3865−3868.
(32) Sun, J.; Ruzsinszky, A.; Perdew, J. Strongly Constrained and Appropriately Normed Semilocal Density Functional. *Phys. Rev. Lett.* **2015**, *115*, 036402.
(33) Krukau, A. V.; Vydrov, O. A.; Izmaylov, A. F.; Scuseria, G. E. Influence of the Exchange Screening Parameter on the Performance of Screened Hybrid Functionals. *J. Chem. Phys.* **2006**, *125*, 224106.
(34) Clarke, S. J.; Guinot, B. P.; Michie, C. W.; Calmont, M. J. C.; Rosseinsky, M. J. Oxynitride Perovskites: Synthesis and Structures of $LaZrO_2N$, $NdTiO_2N$, and $LaTiO_2N$ and Comparison with Oxide Perovskites. *Chem. Mater.* **2002**, *14*, 288−294.
(35) Abeysinghe, D.; Skrabalak, S. E. Toward Shape-Controlled Metal Oxynitride and Nitride Particles for Solar Energy Applications. *ACS Energy Lett.* **2018**, *3*, 1331−1344.
(36) Ishizawa, N.; Ninomiya, K.; Sakakura, T.; Wang, J. Redetermination of $Nd_2Ti_2O_7$: A Non-Centrosymmetric Structure with Perovskite-Type Slabs. *Acta Crystallogr., Sect. E: Struct. Rep. Online* **2013**, *69*, i19−i19.
(37) Reddy, Y. S.; Kistaiah, P.; Vishnuvardhan Reddy, C. Elastic Properties of Double Layered Manganites $R_{1.2}Sr_{1.8}Mn_2O_7$ (R = La, Pr, Nd, Sm). *Rare Met.* **2014**, *33*, 166−170.
(38) Joseph, L. K.; Dayas, K. R.; Damodar, S.; Krishnan, B.; Krishnankutty, K.; Nampoori, V. P. N.; Radhakrishnan, P. Photoluminescence Studies on Rare Earth Titanates Prepared by Self-Propagating High Temperature Synthesis Method. *Spectrochim. Acta, Part A* **2008**, *71*, 1281−1285.
(39) Ma, Z.; Dronskowski, R.; Slabon, A.; Jaworski, A. Paramagnetic ^{14}N MAS NMR without Paramagnetic Shifts: Remarkable Lattice of $LaTiO_2N$ and $CeTiO_2N$ Oxynitride Perovskites. *ChemRxiv* **2020**.
(40) Seibel II, H. A.; Karen, P.; Wagner, T. R.; Woodward, P. M. Synthesis and Characterization of Color Variants of Nitrogen- and Fluorine-Substituted TiO_2. *J. Mater. Chem.* **2009**, *19*, 471−477.
(41) Wang, X.; Hisatomi, T.; Liang, J.; Wang, Z.; Xiang, Y.; Zhao, Y.; Dai, X.; Takata, T.; Domen, K. Facet Engineering of $LaNbON_2$ Transformed from $LaKNaNbO_5$ for Enhanced Photocatalytic O_2 Evolution. *J. Mater. Chem. A* **2020**, *8*, 11743−11751.
(42) Kim, Y.-I.; Woodward, P. M.; Baba-Kishi, K. Z.; Tai, C. W. Characterization of the Structural, Optical, and Dielectric Properties of Oxynitride Perovskites AMO_2N (A = Ba, Sr, Ca; M = Ta, Nb). *Chem. Mater.* **2004**, *16*, 1267−1276.
(43) Ma, Z.; Jaworski, A.; George, J.; Rokicinska, A.; Thersleff, T.; Budnyak, T. M.; Hautier, G.; Pell, A. J.; Dronskowski, R.; Kuśtrowski, P.; Slabon, A. Exploring the Origins of Improved Photocurrent by Acidic Treatment for Quaternary Tantalum-Based Oxynitride Photoanodes on the Example of $CaTaO_2N$. *J. Phys. Chem. C* **2020**, *124*, 152−160.
(44) Gelderman, K.; Lee, L.; Donne, S. W. Flat-Band Potential of a Semiconductor: Using the Mott−Schottky Equation. *J. Chem. Educ.* **2007**, *84*, 685.
(45) Ma, Z.; Linnenberg, O.; Rokicinska, A.; Kustrowski, P.; Slabon, A. Augmenting the Photocurrent of $CuWO_4$ Photoanodes by Heat Treatment in the Nitrogen Atmosphere. *J. Phys. Chem. C* **2018**, *122*, 19281−19288.
(46) Mao, L.; Cai, X.; Gao, H.; Diao, X.; Zhang, J. A Newly Designed Porous Oxynitride Photoanode with Enhanced Charge Carrier Mobility. *Nano Energy* **2017**, *39*, 172−182.
(47) Ammari, A.; Trari, M. Electronic States in Tin Oxide Thin Films upon Photo and Electrochemical Analysis. *Colloids Surf., A* **2019**, *561*, 178−186.
(48) Harikesh, P. C.; Wu, B.; Ghosh, B.; John, R. A.; Lie, S.; Thirumal, K.; Wong, L. H.; Sum, T. C.; Mhaisalkar, S.; Mathews, N. Doping and Switchable Photovoltaic Effect in Lead-Free Perovskites Enabled by Metal Cation Transmutation. *Adv. Mater.* **2018**, *30*, 1802080.
(49) Chang-Ha, K.; Su-Il, P.; Eung-Jo, L. Donor Distribution over Anodically Passivating Crystalline and Amorphous TiO_2 Films. *Mater. Lett.* **1991**, *10*, 387−391.
(50) Schoonman, J.; Vos, K.; Blasse, G. Donor Densities in TiO_2 Photoelectrodes. *J. Electrochem. Soc.* **1981**, *128*, 1154.

https://dx.doi.org/10.1021/acs.inorgchem.0c03041
Inorg. Chem. 2021, 60, 919−929

(51) M Ganose, A.; J Jackson, A.; O Scanlon, D. Sumo: Command-Line Tools for Plotting and Analysis of Periodic Ab Initio Calculations. *J. Open Source Softw.* **2018**, *3*, 717.
(52) Slabon, A.; Mensing, C.; Kubata, C.; Cuervo-Reyes, E.; Nesper, R. Field-Induced Inversion of the Magnetoresistive Effect in the Zintl Phase $Eu_{5+x}Mg_{18-x}Si_{13}$ (x = 2.2). *Angew. Chem., Int. Ed.* **2013**, *52*, 2122−2125.
(53) Chen, K.; Dronskowski, R. First-Principles Study of Divalent 3d Transition-Metal Carbodiimides. *J. Phys. Chem. A* **2019**, *123*, 9328−9335.
(54) Barreca, D.; Gasparotto, A.; Lebedev, O. I.; Maccato, C.; Pozza, A.; Tondello, E.; Turner, S.; Van Tendeloo, G. Controlled Vapor-Phase Synthesis of Cobalt Oxide Nanomaterials with Tuned Composition and Spatial Organization. *CrystEngComm* **2010**, *12*, 2185.
(55) King, B. R.; Patel, H. C.; Gulino, D. A.; Tatarchuk, B. J. Kinetic Measurements of Oxygen Dissolution into Niobium Substrates: In Situ X-Ray Photoelectron Spectroscopy Studies. *Thin Solid Films* **1990**, *192*, 351−369.
(56) Meng, F.; Hong, Z.; Arndt, J.; Li, M.; Zhi, M.; Yang, F.; Wu, N. Visible Light Photocatalytic Activity of Nitrogen-Doped $La_2Ti_2O_7$ Nanosheets Originating from Band Gap Narrowing. *Nano Res.* **2012**, *5*, 213−221.
(57) Wang, C.; Hu, Q.; Huang, J.; Wu, L.; Deng, Z.; Liu, Z.; Liu, Y.; Cao, Y. Efficient Hydrogen Production by Photocatalytic Water Splitting Using N-Doped TiO_2 Film. *Appl. Surf. Sci.* **2013**, *283*, 188−192.
(58) Masuda, Y.; Mashima, R.; Yamada, M.; Ikeuchi, K.; Murai, K.; Waterhouse, G. I. N.; Metson, J. B.; Moriga, T. Relationship between Anion and Cation Nonstoichiometries and Valence State of Titanium in Perovskite-Type Oxynitrides $LaTiO_2N$. *J. Ceram. Soc. Jpn.* **2009**, *117*, 76−81.
(59) Trujillo-Navarrete, B.; Paraguay-Delgado, F.; Pérez-Sicairos, S. Structure, Microstructure and Surface of Nd^{3+}-Doped Mesoporous Anatase-Phase TiO_2. *Appl. Phys. A: Mater. Sci. Process.* **2020**, *126*, 592.
(60) Li, W.; Frenkel, A. I.; Woicik, J. C.; Ni, C.; Shah, S. I. Dopant Location Identification in Nd^{3+}-Doped TiO_2 Nanoparticles. *Phys. Rev. B: Condens. Matter Mater. Phys.* **2005**, *72*, 155315.
(61) Higashi, M.; Domen, K.; Abe, R. Fabrication of Efficient TaON and Ta_3N_5 Photoanodes for Water Splitting under Visible Light Irradiation. *Energy Environ. Sci.* **2011**, *4*, 4138.
(62) Gujral, S. S.; Simonov, A. N.; Higashi, M.; Abe, R.; Spiccia, L. Optimization of Titania Post-Necking Treatment of TaON Photoanodes to Enhance Water-Oxidation Activity under Visible-Light Irradiation. *ChemElectroChem.* **2015**, *2*, 1270−1278.
(63) Sambur, J. B.; Chen, T.-Y.; Choudhary, E.; Chen, G.; Nissen, E. J.; Thomas, E. M.; Zou, N.; Chen, P. Sub-Particle Reaction and Photocurrent Mapping to Optimize Catalyst-Modified Photoanodes. *Nature* **2016**, *530*, 77−80.
(64) Hahn, N. T.; Mullins, C. B. Photoelectrochemical Performance of Nanostructured Ti- and Sn-Doped α-Fe_2O_3 Photoanodes. *Chem. Mater.* **2010**, *22*, 6474−6482.
(65) Oh, K.; Dorcet, V.; Fabre, B.; Loget, G. Dissociating Water at N-Si Photoanodes Partially Covered with Fe Catalysts. *Adv. Energy Mater.* **2020**, *10*, 1902963.
(66) Kuang, Y.; Jia, Q.; Ma, G.; Hisatomi, T.; Minegishi, T.; Nishiyama, H.; Nakabayashi, M.; Shibata, N.; Yamada, T.; Kudo, A.; Domen, K. Ultrastable Low-Bias Water Splitting Photoanodes via Photocorrosion Inhibition and in Situ Catalyst Regeneration. *Nat. Energy* **2017**, *2*, 16191.
(67) Liardet, L.; Katz, J. E.; Luo, J.; Grätzel, M.; Hu, X. An Ultrathin Cobalt-Iron Oxide Catalyst for Water Oxidation on Nanostructured Hematite Photoanodes. *J. Mater. Chem. A* **2019**, *7*, 6012−6020.
(68) Higashi, M.; Domen, K.; Abe, R. Highly Stable Water Splitting on Oxynitride TaON Photoanode System under Visible Light Irradiation. *J. Am. Chem. Soc.* **2012**, *134*, 6968−6971.
(69) Pei, L.; Wang, H.; Wang, X.; Xu, Z.; Yan, S.; Zou, Z. Nanostructured $TaON/Ta_3N_5$ as a Highly Efficient Type-II Heterojunction Photoanode for Photoelectrochemical Water Splitting. *Dalt. Trans.* **2018**, *47*, 8949−8955.
(70) Lee, S. A.; Lee, T. H.; Kim, C.; Choi, M.-J.; Park, H.; Choi, S.; Lee, J.; Oh, J.; Kim, S. Y.; Jang, H. W. Amorphous Cobalt Oxide Nanowalls as Catalyst and Protection Layers on n-Type Silicon for Efficient Photoelectrochemical Water Oxidation. *ACS Catal.* **2020**, *10*, 420−429.
(71) Liang, J.; Wang, N.; Zhang, Q.; Liu, B.; Kong, X.; Wei, C.; Zhang, D.; Yan, B.; Zhao, Y.; Zhang, X. Exploring the Mechanism of a Pure and Amorphous Black-Blue TiO_2:H Thin Film as a Photoanode in Water Splitting. *Nano Energy* **2017**, *42*, 151−156.
(72) Hagfeldt, A.; Lindström, H.; Södergren, S.; Lindquist, S.-E. Photoelectrochemical Studies of Colloidal TiO_2 Films: The Effect of Oxygen Studied by Photocurrent Transients. *J. Electroanal. Chem.* **1995**, *381*, 39−46.
(73) Moir, J. W.; Sackville, E. V.; Hintermair, U.; Ozin, G. A. Kinetics versus Charge Separation: Improving the Activity of Stoichiometric and Non-Stoichiometric Hematite Photoanodes Using a Molecular Iridium Water Oxidation Catalyst. *J. Phys. Chem. C* **2016**, *120*, 12999−13012.
(74) Le Formal, F.; Sivula, K.; Grätzel, M. The Transient Photocurrent and Photovoltage Behavior of a Hematite Photoanode under Working Conditions and the Influence of Surface Treatments. *J. Phys. Chem. C* **2012**, *116*, 26707−26720.
(75) Du, C.; Zhang, M.; Jang, J.-W.; Liu, Y.; Liu, G.-Y.; Wang, D. Observation and Alteration of Surface States of Hematite Photoelectrodes. *J. Phys. Chem. C* **2014**, *118*, 17054−17059.
(76) Liu, Y.; Guijarro, N.; Sivula, K. Understanding Surface Recombination Processes Using Intensity-Modulated Photovoltage Spectroscopy on Hematite Photoanodes for Solar Water Splitting. *Helv. Chim. Acta* **2020**, *103*, No. e2000064.
(77) Ye, K.-H.; Li, H.; Huang, D.; Xiao, S.; Qiu, W.; Li, M.; Hu, Y.; Mai, W.; Ji, H.; Yang, S. Enhancing Photoelectrochemical Water Splitting by Combining Work Function Tuning and Heterojunction Engineering. *Nat. Commun.* **2019**, *10*, 3687.

https://dx.doi.org/10.1021/acs.inorgchem.0c03041
Inorg. Chem. 2021, 60, 919−929